



Preparation of $\text{Nd}_2\text{Fe}_{14}\text{B}/\text{C}$ magnetic powder and its application in proton exchange membrane fuel cells



Jicheng Shi, Hongfeng Xu*, Hong Zhao, Lu Lu, Xiaoxin Wu

College of Environmental and Chemical Engineering, Dalian Jiaotong University, Dalian 116028, Liaoning Province, PR China

HIGHLIGHTS

- The magnetic electrode has higher C_d and lower R_{ct} than the nonmagnetic electrode.
- The magnetic field of $\text{Nd}_2\text{Fe}_{14}\text{B}/\text{C}$ increases the oxygen diffusion/transfer coefficient.
- The magnetic interactions among magnetic particles decrease PEMFC performance.
- The carbon particles in $\text{Nd}_2\text{Fe}_{14}\text{B}/\text{C}$ decrease the cathode ohmic polarization of PEMFCs.
- The magnetic field generated from $\text{Nd}_2\text{Fe}_{14}\text{B}/\text{C}$ promotes oxygen transfer.

ARTICLE INFO

Article history:

Received 2 August 2013

Received in revised form

14 November 2013

Accepted 28 November 2013

Available online 11 December 2013

Keywords:

Magnetic powder

Magnetic field

Electric double-layer capacitance

Charge-transfer resistance

Oxygen diffusion coefficient

Oxygen transfer coefficient

ABSTRACT

$\text{Nd}_2\text{Fe}_{14}\text{B}$ and $\text{Nd}_2\text{Fe}_{14}\text{B}/\text{C}$ magnetic powders are prepared by the ball-milling and high-temperature baking methods, respectively. The effect of the magnetic powder in the oxygen transfer process is studied using the three-electrode electrochemical system, rotating disk glassy carbon electrode, and proton exchange membrane fuel cells (PEMFCs). Results show that the magnetic electrode has higher electric double-layer capacitance and lower charge-transfer resistance than the nonmagnetic electrode at different $\text{Nd}_2\text{Fe}_{14}\text{B}/\text{C}$ load densities. In addition, the oxygen diffusion coefficient and transfer coefficient for the magnetic electrode are both larger than the nonmagnetic electrode. At 0.40 mg cm^{-2} $\text{Nd}_2\text{Fe}_{14}\text{B}/\text{C}$ load density in the PEMFC cathode, the magnetic PEMFC discharge current increases by 39.874% compared with the nonmagnetic PEMFC at 0.20 V discharge voltage. The magnetic PEMFC discharge performance at 0.80 mg cm^{-2} $\text{Nd}_2\text{Fe}_{14}\text{B}/\text{C}$ load density is lower than the magnetic PEMFC at 0.40 mg cm^{-2} load density. These factors result in the decline of magnetic PEMFC discharge performance at higher $\text{Nd}_2\text{Fe}_{14}\text{B}/\text{C}$ load density, including decreased Pt/C actual catalyst area and increased magnetic interactions among different magnetic particles.

© 2013 Elsevier B.V. All rights reserved.

1. Introduction

Atmospheric air is the oxidant in the cathode of proton exchange membrane fuel cells (PEMFCs). However, unfavorable factors affect the use of air as an oxidant. First, given that the oxygen concentration is only 21% in atmospheric air, the open circuit potential of single cell is about 10 mV lower than that at normal pressure conditions. Second, other ingredients in the air may occupy certain catalytic active sites at the catalyst layer during the air diffusion process. This condition inhibits the oxygen reduction reaction (ORR) at the catalyst surface, and leads to the cathode

electrochemical polarization, thereby decreasing the discharge performance of PEMFCs [1].

In the magnetic field, oxygen and nitrogen molecules have different moving trajectories. Oxygen molecules move in the direction of increased magnetic strength and magnetic field gradient, whereas nitrogen molecules move toward the decreased magnetic strength and magnetic field gradient direction. Magnetic strength and magnetic field gradient increase as the oxygen molecules move closer to the magnetic particles. Therefore, these molecules are enriched near the magnetic particles, i.e., the oxygen molecular concentration is increased at the magnetic particle surface (Fig. 1).

Cai et al. studied the oxygen enrichment from air in a gradient magnetic field generated at the edge of a permanent magnet, and found that the oxygen concentration increments was up to 0.65% when the air flux was $40, 20 \text{ cm}^3 \text{ min}^{-1}$ into and out of the

* Corresponding author. Tel.: +86 411 84106713; fax: +86 411 84106723.
E-mail address: hfxu@fuelcell.com.cn (H. Xu).

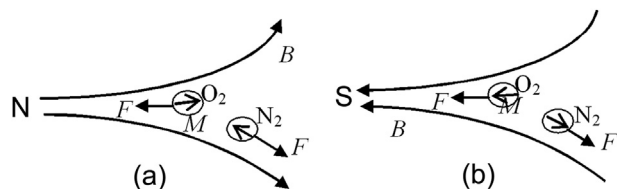


Fig. 1. Oxygen and nitrogen molecule separation in the magnetic field. (a) North and (b) south poles of the magnet.

magnetic field [2]. Aleksandra Rybak reported that the oxygen concentration increases from 21% to 56% when the air (atmospheric pressure) flows through the neodymium powder/ethyl cellulose membrane with a magnetic strength of 2.25 mT [3]. Wang et al. studied the function of the magnetic force on oxygen transfer process in PEMFC catalyst layer through the numerical simulation method, and found that the magnetic force generated from the magnetic particles (diameter 5 μm) affects the oxygen transfer process, increases the air flow rate at the electrode interface, and promotes the oxygen molecules transfer to the catalytic reaction zones [4].

Magnetic strength affects the oxygen transfer rate in the electrode. This paper first prepared the $\text{Nd}_2\text{Fe}_{14}\text{B}$ magnetic powder, and then used the carbon coating to improve the corrosion resistance and conductivity properties of the magnetic particles. Finally, the effectiveness of the $\text{Nd}_2\text{Fe}_{14}\text{B}/\text{C}$ magnetic powder on the oxygen transfer process was tested through the three-electrode electrochemical system, the rotating disk electrode, and the PEMFC.

2. Experimental

2.1. $\text{Nd}_2\text{Fe}_{14}\text{B}$ and $\text{Nd}_2\text{Fe}_{14}\text{B}/\text{C}$ magnetic powder preparation

$\text{Nd}_2\text{Fe}_{14}\text{B}$ magnetic powder was prepared through the ball-milling method. First, $\text{Nd}_2\text{Fe}_{14}\text{B}$ magnetic blocks (10 mm \times 5 mm, Tianjin Davies, China) were demagnetized on the red-hot surface at the electric furnace. Afterward, the blocks were broken into the small pieces using a hammer and ball-milled at 200 rpm for 30 h in a ball grinding mill (ND7, Tianjin Nanda Tianzun, China). The prepared $\text{Nd}_2\text{Fe}_{14}\text{B}$ powder was sieved by a sample sieve and preserved in anhydrous ethanol.

The prepared $\text{Nd}_2\text{Fe}_{14}\text{B}$ magnetic powder was placed into 1 g mL^{-1} starch solution and stirred for 1 h at high-speed. The slurry was then dried in the drying oven at 110 $^{\circ}\text{C}$ to remove the water. Under the protection of nitrogen, the black $\text{Nd}_2\text{Fe}_{14}\text{B}/\text{C}$ material was prepared in the vacuum microwave sintering furnace (NJZ4-3B, Nanjing Jiequan, China) at 1100 $^{\circ}\text{C}$ for 2 h.

2.2. Magnetic powder characterization

The morphology was observed using a scanning electron microscope (JSM-6360LV, JEOL, Japan). The XRD patterns of the samples were obtained using an X-ray diffractometer (D/max2400, Rigaku, Japan) with $\text{Cu K}\alpha$ radiation (0.1542 nm) in the 2θ range of 20 $^{\circ}$ –70 $^{\circ}$. The magnetic properties were tested with a vibrating sample magnetometer (JDM-13, Changchun Tongzhou, China).

2.3. Corrosion resistance of $\text{Nd}_2\text{Fe}_{14}\text{B}/\text{C}$ material in 0.5 M H_2SO_4

$\text{Nd}_2\text{Fe}_{14}\text{B}$ and $\text{Nd}_2\text{Fe}_{14}\text{B}/\text{C}$ materials were separately immersed in 50 mL of 0.5 M H_2SO_4 , and the magnetic response was tested in

350 mT magnetic field at different times. $\text{Nd}_2\text{Fe}_{14}\text{B}/\text{C}$ and $\text{Nd}_2\text{Fe}_{14}\text{B} + \text{C}$ ($\text{Nd}_2\text{Fe}_{14}\text{B}:\text{carbon} = 11:7$) materials were separately loaded on the graphite electrode, and the load density was 0.80 mg cm^{-2} . A blank graphite sheet was used as the counter electrode. The reference electrode was the saturated calomel electrode (SCE), and the electrolyte was 0.5 M H_2SO_4 with nitrogen saturation. The corrosion potential and the corrosion current were tested through an electrochemical workstation (CHI660C, Shanghai Chenhua, China).

2.4. Electrochemical experiments for oxygen reduction reaction

2.4.1. Three-electrode electrochemical system

Electrochemical experiments were conducted in an electrochemical workstation. A certain amount of $\text{Nd}_2\text{Fe}_{14}\text{B}/\text{C}$, 50% Pt/C (Dalian Sunrise Power, China), and 5% Nafion (Dupont, USA) were homogeneously mixed by ultrasonication. The homogeneous solutions were loaded on the graphite sheet under a 350 mT magnetic field and served as the working electrode. Another blank graphite sheet served as the counter electrode, and a saturated calomel electrode (SCE) was used as the reference electrode. H_2SO_4 (0.5 M) was used as the electrolyte under continuous air saturation. After loading the magnetic particles and the Pt/C catalyst on the working electrode, the electrode was magnetized in a 2 T magnetic field using a magnetizing machine (TSK-H1540, Nanjing Tingjin, China), thereby obtaining the magnetic electrode. An unmagnetized electrode, called the nonmagnetic electrode, was used for comparison. The electrochemical performance of $\text{Nd}_2\text{Fe}_{14}\text{B}/\text{C}$ and its effect on oxygen transfer were evaluated in a three-electrode glass cell through different measurements, namely, CV with a scan rate of 10 mV s^{-1} ; the Tafel test from 1.2 V to 0.40 V (vs. SCE) at a scan rate of 10 mV s^{-1} ; the small triangular waveform sweep from 0.80 V to 0.79 V (vs. SCE) at a scan rate of 100 V s^{-1} ; the multi-current step with successive steps of -0.01 , -0.1 , -1 , -10 , and -100 mA; and the multi-potential steps between 1.0 V and 0.40 V (vs. SCE) at a step of -0.20 V each.

2.4.2. Rotating disk glassy carbon electrode experiment

The glassy carbon electrode ($d = 3$ mm) was pretreated by 5# metallographic sandpaper and 0.5 μm of Al_2O_3 polishing powder, and then washed two times with distilled water. Afterward, the glassy carbon electrode was immersed in methanol for ultrasonic cleaning. Finally, 50 cycles of CV scan was performed on the glassy carbon electrode from -0.20 V to 1.0 V (vs. SCE) with the scan rate of 50 mV s^{-1} in 0.5 M H_2SO_4 .

The 50% Pt/C catalyst and $\text{Nd}_2\text{Fe}_{14}\text{B}/\text{C}$ powders load density were both 0.80 mg cm^{-2} in the rotating disk glassy carbon electrode. The solution was composed of 5 mg of catalyst, 50 μL of Nafion, and 1 mL of anhydrous ethanol. A certain amount of the solution was loaded on the glassy carbon electrode under 350 mT magnetic field, and the electrode was then dried at 80 $^{\circ}\text{C}$ for 1 h. The magnetic rotating disk glassy carbon electrode was obtained through $\text{Nd}_2\text{Fe}_{14}\text{B}/\text{C}$ magnetization under 2 T magnetic strength. A platinum wire was used as auxiliary electrode, SCE was used as reference electrode, and the electrolyte was 0.5 M H_2SO_4 with air saturation. The test method was the linear sweep voltammetry with the scan speed of 5 mV s^{-1} from 1.0 V to -0.20 V.

2.5. Discharge performance of PEMFC with $\text{Nd}_2\text{Fe}_{14}\text{B}/\text{C}$ in the cathode

A certain amount of 50% Pt/C catalyst, $\text{Nd}_2\text{Fe}_{14}\text{B}/\text{C}$ powder, Nafion solution, and anhydrous ethanol were mixed homogeneously by ultrasonic vibration. The black ink was then sprayed on the diffusion layer of the Toray carbon paper (1 \times 5 cm^2). The 50%

Pt/C load density was 0.80 mg cm^{-2} in the PEMFC cathode and anode. The $\text{Nd}_2\text{Fe}_{14}\text{B/C}$ load density was $0.40, 0.80 \text{ mg cm}^{-2}$ in the PEMFC cathode. The membrane electrode assembly (MEA) includes the polyester frame, anode, Nafion1135 film (DuPont, USA), cathode, and another polyester frame. The MEA was preheated at 140°C for 60 s in the hot-pressing machine, and then pressed for 60 s at 10 MPa. Finally, the MEA was finished and assembled into a single cell. The discharge performance of the single cell was tested using the PEMFC test platform (FCTS-5000, Sunrise Power, China). The hydrogen and air entrance pressure were both 0.11 MPa. The humidification and PEMFC operation temperature was 70°C , respectively.

2.6. Magnetization process of $\text{Nd}_2\text{Fe}_{14}\text{B/C}$ particles on the electrode

The homogeneous solution mixture of $\text{Nd}_2\text{Fe}_{14}\text{B/C}$, 5% Nafion, and ethanol was loaded on the working electrode in a 300 mT magnetic field. Thus, the magnetic powder was attached to the working electrode surface. Then, the magnetic powder was magnetized under 2 T magnetic strength. Fig. 2 shows the magnetization process of the magnetic particles. As the magnetic particles were loaded on the working electrode, the magnetic moment (M) of each magnetic domain was oriented at 300 mT magnetic field. Therefore, the particle's magnetic poles were polarized (Fig. 2(b)). The high coercivity of the $\text{Nd}_2\text{Fe}_{14}\text{B/C}$ material resulted in reversible movement of the magnetic domain walls at 300 mT magnetic field. After the magnetic field was removed, the magnetic particles remained in demagnetized state, i.e., they do not display magnetic property (Fig. 2(a)), which is the nonmagnetic $\text{Nd}_2\text{Fe}_{14}\text{B/C}$. With the 2 T magnetic strength from the magnetizing machine, the aligned magnetic particles were instantly magnetized; each magnetic domain wall was irreversibly moved. The magnetic particle was eventually magnetized to saturation (Fig. 2(c) and (e)). The magnetic moment (M) direction of $\text{Nd}_2\text{Fe}_{14}\text{B/C}$ particles depended on the magnetization direction (Fig. 2(c) and (e)). After the removal of the external magnetic field, the magnetic materials retained their magnetic properties because of their single domain structures, which are the magnetic $\text{Nd}_2\text{Fe}_{14}\text{B/C}$ powders (Fig. 2(d) and (f)).

3. Results and discussion

3.1. Morphological characterization of $\text{Nd}_2\text{Fe}_{14}\text{B}$ and $\text{Nd}_2\text{Fe}_{14}\text{B/C}$ magnetic powders

Fig. 3 shows the images of $\text{Nd}_2\text{Fe}_{14}\text{B}$ and $\text{Nd}_2\text{Fe}_{14}\text{B/C}$ materials. The morphology of the $\text{Nd}_2\text{Fe}_{14}\text{B}$ particles is irregular and the

diameter is below $1 \mu\text{m}$ after the ball-milling process, as shown in Fig. 3(a). Two kinds of particles have been observed in Fig. 3(b): the $\text{Nd}_2\text{Fe}_{14}\text{B}$ particles with a diameter of 200 nm–300 nm, and the carbon particles with the size of a few nanometers. The carbon coverage on the $\text{Nd}_2\text{Fe}_{14}\text{B}$ surface protects the $\text{Nd}_2\text{Fe}_{14}\text{B}$ particles from air, H^+ , or OH^- corrosions and preserves its magnetic properties in the electrolyte [5–7].

3.2. $\text{Nd}_2\text{Fe}_{14}\text{B}$ and $\text{Nd}_2\text{Fe}_{14}\text{B/C}$ magnetic powder XRD

Fig. 4 shows the XRD patterns of the amorphous carbon, $\text{Nd}_2\text{Fe}_{14}\text{B}$, and $\text{Nd}_2\text{Fe}_{14}\text{B/C}$ materials. To distinguish the XRD curves, the intensity scale of each sample was different. The ordinate of the XRD spectrum did not mark the intensity scale, suggesting the samples' relative diffraction intensity. Fig. 4(b) shows the diffraction intensities in decreasing, where the diffraction peaks at 42.3° , 37.2° , 43.9° , 39.1° , 33.0° , and 26.9° correspond to the (410), (214), (314), (313), (311), and (212) crystal planes of the $\text{Nd}_2\text{Fe}_{14}\text{B}$, respectively. This result is consistent with the tetragonal $\text{Nd}_2\text{Fe}_{14}\text{B}$ phase in the JCPDS 77-1404 standard spectrum. Fig. 4(c) shows the $\text{Nd}_2\text{Fe}_{14}\text{B/C}$ XRD spectrum, where the main diffraction peak correspond to the (410), (214), (314), and (313) crystal planes of $\text{Nd}_2\text{Fe}_{14}\text{B}$ [8].

3.3. Magnetic properties of the $\text{Nd}_2\text{Fe}_{14}\text{B}$ and $\text{Nd}_2\text{Fe}_{14}\text{B/C}$ particles

Fig. 5 shows the hysteresis loops of the $\text{Nd}_2\text{Fe}_{14}\text{B}$ and $\text{Nd}_2\text{Fe}_{14}\text{B/C}$ materials. The coercive force and the residual magnetization of the $\text{Nd}_2\text{Fe}_{14}\text{B}$ material are 171.42 kA m^{-1} and $48.11 \text{ Am}^2 \text{ kg}^{-1}$, respectively. The coercive force and residual magnetization of the $\text{Nd}_2\text{Fe}_{14}\text{B/C}$ material are 146.57 kA m^{-1} and $25.77 \text{ Am}^2 \text{ kg}^{-1}$, respectively. The $\text{Nd}_2\text{Fe}_{14}\text{B/C}$ material has higher coercive force and residual magnetization after the carbon coating process, and the $\text{Nd}_2\text{Fe}_{14}\text{B/C}$ is suitable as a magnetic field source [9]. The magnetic strength of a single magnetic particle is highly weak; thus, the hall probe of the tesla meter is unable to detect its magnetic strength.

3.4. Corrosion resistance of $\text{Nd}_2\text{Fe}_{14}\text{B/C}$ material

After $\text{Nd}_2\text{Fe}_{14}\text{B/C}$ was immersed in 0.5 M H_2SO_4 for a week, several precipitates remained in the acid solution, which exhibited significant magnetic response in 350 mT magnetic field. However, $\text{Nd}_2\text{Fe}_{14}\text{B}$ was rapidly dissolved in 0.5 M H_2SO_4 . Several bubbles appeared in the acid, and the $\text{Nd}_2\text{Fe}_{14}\text{B}$ powders completely disappeared. Fig. 6 presents the relative corrosion potential and corrosion current of $\text{Nd}_2\text{Fe}_{14}\text{B/C}$ and $\text{Nd}_2\text{Fe}_{14}\text{B} + \text{carbon}$ materials. Comparison of the relative corrosion potential showed that

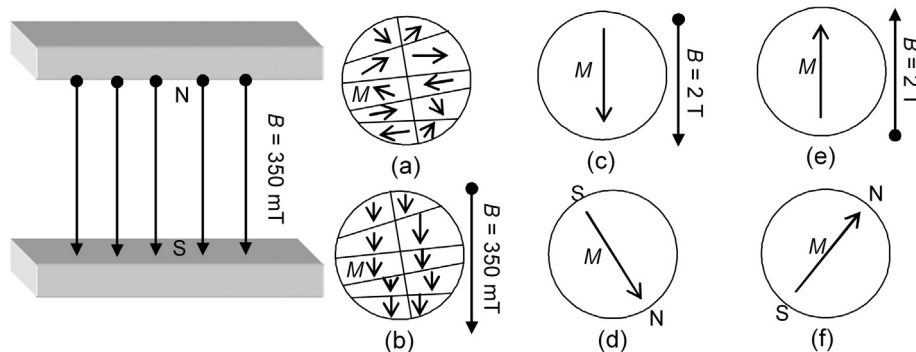


Fig. 2. Magnetization process of $\text{Nd}_2\text{Fe}_{14}\text{B/C}$ magnetic materials. (a) Nonmagnetic particle; (b) nonmagnetic particle in 350 mT magnetic field; (c) magnetizing magnetic particle, vertical downward magnetization direction; (d) magnetization completed magnetic particle, vertical downward magnetization direction; (e) magnetizing magnetic particles, upward vertical magnetization direction; (f) magnetization completed magnetic particle, upward vertical magnetization direction.

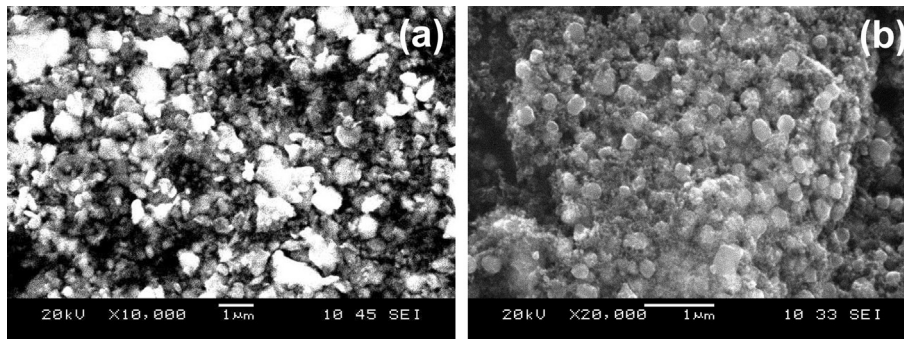


Fig. 3. SEM images of (a) $\text{Nd}_2\text{Fe}_{14}\text{B}$ and (b) $\text{Nd}_2\text{Fe}_{14}\text{B/C}$.

$\text{Nd}_2\text{Fe}_{14}\text{B/C}$ was larger than the $\text{Nd}_2\text{Fe}_{14}\text{B}$ + carbon material (Fig. 6). Compared with the relative corrosion current in Fig. 6, $\text{Nd}_2\text{Fe}_{14}\text{B/C}$ was lower than $\text{Nd}_2\text{Fe}_{14}\text{B}$ + carbon material. The results showed that the carbon coating $\text{Nd}_2\text{Fe}_{14}\text{B}$ material reduced the $\text{Nd}_2\text{Fe}_{14}\text{B}$ corrosion rate in acid, and $\text{Nd}_2\text{Fe}_{14}\text{B/C}$ enhanced the $\text{Nd}_2\text{Fe}_{14}\text{B}$ corrosion resistance property in acidic conditions.

3.5. Three-electrode electrochemical system

Fig. 7 shows CV curves obtained with and without $\text{Nd}_2\text{Fe}_{14}\text{B/C}$ in the electrode, in which the oxygen reduction peak potential and peak current are 0.41 V and 3.36 mA cm^{-2} for the magnetic electrode, respectively, at 0.80 mg cm^{-2} $\text{Nd}_2\text{Fe}_{14}\text{B/C}$ load density. Meanwhile, the oxygen reduction peak potential and peak current for the nonmagnetic electrode are 0.38 V and 1.99 mA cm^{-2} . The oxygen peak current increased by 68.8% for the magnetic electrode than the nonmagnetic electrode, and the peak potential shifted 30 mV toward the noble direction. Using Eq. (1), the variations of the oxygen reduction peak current are only correlated with the oxygen concentration and oxygen diffusion coefficient in the same electrochemical systems in a constant scan rate. The micromagnetic field increases the oxygen bulk concentration or the oxygen diffusion coefficient; thus, the oxygen transfer rate is improved by the magnetic field generated from the $\text{Nd}_2\text{Fe}_{14}\text{B/C}$ magnetization. Similarly, the electrochemical property of the magnetic electrode at $\text{Nd}_2\text{Fe}_{14}\text{B/C}$ load density 1.20 mg cm^{-2} is better than that of the nonmagnetic electrode. Tatsuhiro Okada found that the ORR current increased with the increase in the

magnetic strength after the permanent magnet is placed behind the Pt net or the carbon paper with Pt catalyst [10].

In the irreversible system at 25°C is

$$i_p = 0.4958 F C_O^* D_O^{1/2} \left(\frac{nF}{RT} \right)^{1/2} \nu^{1/2} \quad (1)$$

where i_p is the reduction peak current in the CV curves; C_O^* is oxygen concentration in the bulk solution; D_O is the oxygen diffusion coefficient; and ν is the scan speed.

Without $\text{Nd}_2\text{Fe}_{14}\text{B/C}$ in the electrode, the oxygen reduction peak potential and peak current are 0.41 V and 1.77 mA cm^{-2} , respectively (Fig. 7). The oxygen reduction peak current obtained at 0.80 mg cm^{-2} $\text{Nd}_2\text{Fe}_{14}\text{B/C}$ load density increased by 89.83% compared with that of the Pt/C-only supported electrode. The oxygen reduction peak current of the nonmagnetic electrode increased by 12.43% compared with that obtained without $\text{Nd}_2\text{Fe}_{14}\text{B/C}$ in the electrode. These results indicate that the micromagnetic field from the $\text{Nd}_2\text{Fe}_{14}\text{B/C}$ magnetic powder accelerates oxygen mass transfer and improves the ORR speed. Given that $\text{Nd}_2\text{Fe}_{14}\text{B}$ is composed of rare earth and transition metal elements, it may play a catalytic role in the oxygen reduction process. The transition metal/porous carbon catalyst has high catalytic activity in the ORR process [11–13].

Compared with the magnetic electrode at different $\text{Nd}_2\text{Fe}_{14}\text{B/C}$ load densities, the oxygen reduction peak current at $\text{Nd}_2\text{Fe}_{14}\text{B/C}$ 0.80 mg cm^{-2} is greater than that at 1.20 mg cm^{-2} (Fig. 7). This result may be attributed to two reasons. First, with increased magnetic powder load density, the magnetic field from different magnetic particles interferes with each other, which weakens the

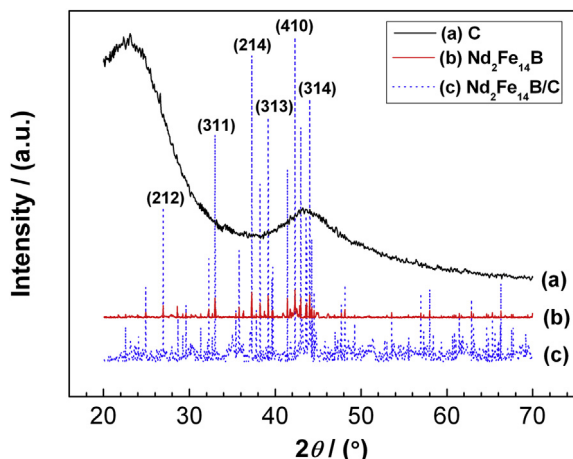


Fig. 4. XRD patterns of (a) carbon, (b) $\text{Nd}_2\text{Fe}_{14}\text{B}$, and (c) $\text{Nd}_2\text{Fe}_{14}\text{B/C}$.

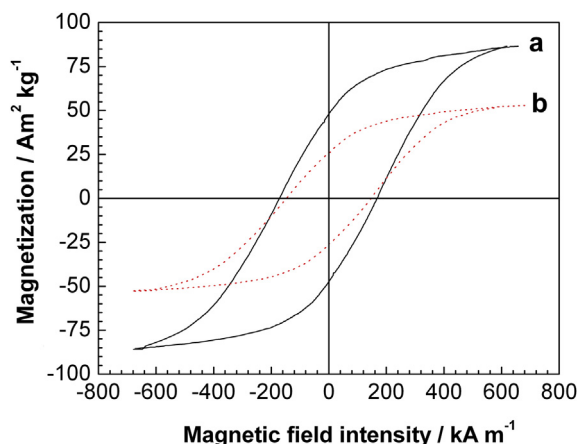


Fig. 5. Hysteresis loops of (a) $\text{Nd}_2\text{Fe}_{14}\text{B}$ and (b) $\text{Nd}_2\text{Fe}_{14}\text{B/C}$.

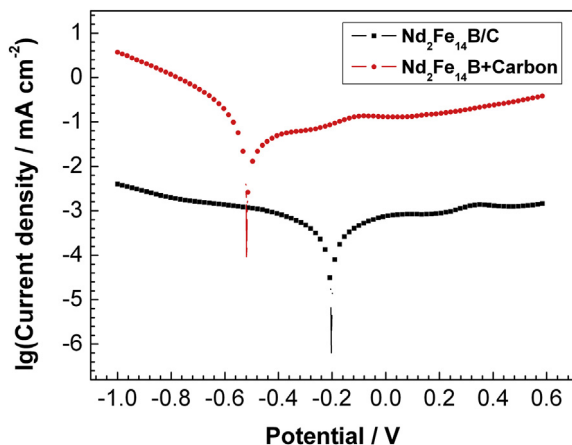


Fig. 6. Corrosion resistance of $\text{Nd}_2\text{Fe}_{14}\text{B/C}$ and $\text{Nd}_2\text{Fe}_{14}\text{B} + \text{carbon}$ material. Scan rate, 5 mV s^{-1} ; electrolyte, $0.5 \text{ M H}_2\text{SO}_4$ with nitrogen saturation.

magnetic order of the single magnetic particles and reduces the effectiveness of magnetic field on oxygen transfer process. Second, the effective Pt/C catalytic area decreased with the increase in magnetic powder load density because of the $\text{Nd}_2\text{Fe}_{14}\text{B/C}$ particle

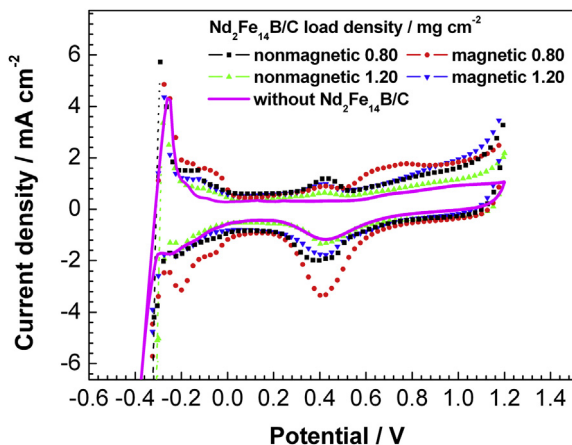


Fig. 7. Cyclic voltammograms of the nonmagnetic and magnetic electrode at different $\text{Nd}_2\text{Fe}_{14}\text{B/C}$ load densities. Scan rate, 10 mV s^{-1} ; electrolyte, $0.5 \text{ M H}_2\text{SO}_4$ with air saturation.

coverage on Pt/C surface, which leads to the decrease in the ORR rate. J.C. Shi et al. found that the discharge performance of zinc-air battery drops with increased magnetic powders in the cathode [14].

The $\text{Nd}_2\text{Fe}_{14}\text{B/C}$ particles were magnetized in 2 T magnetic field, and each magnetic particle served as a small magnet. The N and S pole directions of the different magnetic particles were consistent with each other. Magnetic interaction did not exist among the magnetic particles with $\text{Nd}_2\text{Fe}_{14}\text{B/C}$ load density of 0.80 mg cm^{-2} (Fig. 8(a)). Each magnetic particle could efficiently enrich oxygen. When the magnetic powder load density was large, such as 1.20 mg cm^{-2} , the magnetic field overlapped among the different magnetic particles (Fig. 8(b)). The overlapping magnetic field was similar to the gradually approaching two-strip magnets with the N and S poles opposite each other. The repulsive force gradually increased, indicating the existence of an overlapping magnetic field among the different magnetic particles. When the oxygen molecules were in the superimposed magnetic field, the magnetic force may have been distorted by the complicated magnetic field so they canceled out each other. Thereby, the oxygen transfer effect was reduced at high-magnetic powder load density. The ORR current at 1.20 mg cm^{-2} was less than the current at 0.80 mg cm^{-2} for the magnetic $\text{Nd}_2\text{Fe}_{14}\text{B/C}$.

Comparison of the hydrogen adsorption/desorption currents in the CV curves (Fig. 7) shows that the current from the electrode with $\text{Nd}_2\text{Fe}_{14}\text{B/C}$ is larger than that from the electrode without $\text{Nd}_2\text{Fe}_{14}\text{B/C}$, which indicates that the micromagnetic field in the magnetic electrode increases the number of active Pt/C catalyst sites. This result may be attributed to several reasons. First, the magnetic field accelerates the charge-transfer process and promotes the hydrogen evolution reaction at the graphite electrode. Second, magnetic fields with a certain intensity can improve oxidation–desorption activity through magnetic repulsive forces toward the diamagnetic hydrogen atoms. Z.P. Lu et al. observed that magnetic fields promote the charge-transfer process and improve the speed of hydrogen evolution in the hydrogen reduction reaction at the iron electrode in acidic solution [15]. Third, Fe–B structures in the $\text{Nd}_2\text{Fe}_{14}\text{B}$ crystals may function as assistant catalysts in the hydrogen electrochemical reaction [16]. Thus, the hydrogen adsorption/oxidation current is larger in the magnetic and nonmagnetic electrodes than in the Pt/C catalyst-only electrode.

Fig. 9 shows the Tafel curves of the magnetic and nonmagnetic electrode. At the same $\text{Nd}_2\text{Fe}_{14}\text{B/C}$ load density, the relative equilibrium potential is higher for the magnetic electrode than the nonmagnetic electrode. At the equilibrium state, the relationship between the equilibrium potential and the exchange current

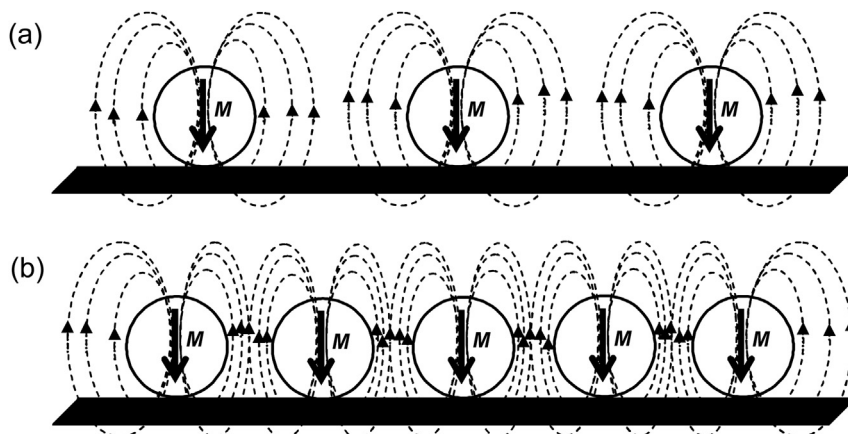


Fig. 8. Magnetic field distribution at different magnetic powder load densities on the electrode. (a) Without and (b) with magnetic interaction among magnetic particles.

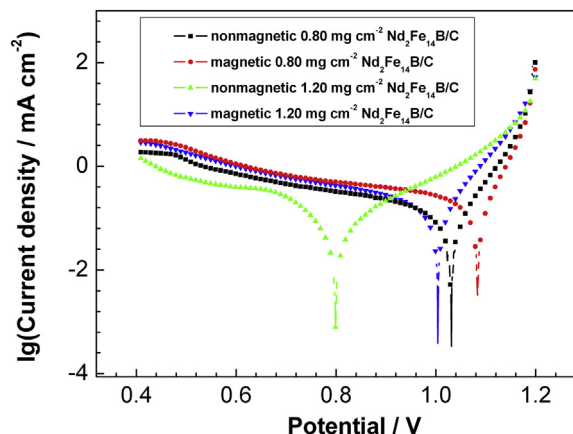
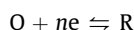


Fig. 9. Tafel curves of the nonmagnetic and magnetic electrode at different $\text{Nd}_2\text{Fe}_{14}\text{B/C}$ load densities. Scan rate, 10 mV s^{-1} ; electrolyte, $0.5 \text{ M H}_2\text{SO}_4$ with air saturation.

density is given in Eqs. (2) and (3). Without concentration polarization, the micro-magnetic field increases the oxygen concentration in the bulk solution; thus, the electrochemical property of the magnetic electrode is higher than that of the nonmagnetic electrode. Hiromu Sakurai also reported that the magnetic field alters the oxygen concentration in the aqueous solution [17].

An electrochemical reaction in the equilibrium state is given by



$$E = E^\theta + \frac{RT}{nF} \ln \left(\frac{C_{\text{O}}^*}{C_{\text{R}}^*} \right) \quad (2)$$

$$\vec{i}^\theta = \overleftarrow{i}^\theta = nFAk_f C_{\text{O}}^* (i = 0) \quad (3)$$

where E is the equilibrium potential; E^θ is the standard electrode potential; k_f is the ORR constant; C_{O}^* is the oxygen concentration in the bulk solution; and i^θ is the exchange current density.

The magnetic electrode at 0.80 mg cm^{-2} has a higher relative equilibrium potential than that at 1.20 mg cm^{-2} $\text{Nd}_2\text{Fe}_{14}\text{B/C}$ load density. The magnetic interaction among different magnetic particles weakens the effectiveness of the magnetic field on the oxygen transfer process, which is the reason for the lower electrochemical properties at higher $\text{Nd}_2\text{Fe}_{14}\text{B/C}$ load density.

Compared with the equilibrium potential difference (ΔE) between the magnetic and nonmagnetic electrodes, the ΔE at 1.20 mg cm^{-2} was larger than the ΔE at 0.80 mg cm^{-2} . At $\text{Nd}_2\text{Fe}_{14}\text{B/C}$ of 1.20 mg cm^{-2} in the electrode, the decrease in Pt/C catalytic activity area became the leading factor in influencing electrode

performance. Therefore, the equilibrium potential of nonmagnetic 1.20 mg cm^{-2} became very low, whereas the equilibrium potential of magnetic 1.20 mg cm^{-2} did not significantly reduce because of its magnetic field effects on oxygen transfer. Therefore, the ΔE value at 1.20 mg cm^{-2} was larger than that at 0.80 mg cm^{-2} between the magnetic and nonmagnetic electrodes.

Fig. 10(a), (b), and (c) shows the small triangular waveform scan, the multi-current step, and the multi-potential step curves of the magnetic and nonmagnetic electrode. As shown in Fig. 10(a), the electric double-layer capacitance (C_d) and the charge-transfer resistance (R_{ct}) are calculated according to the Eqs. (4) and (5) and listed in Table 1. As shown in Table 1, at 0.80 mg cm^{-2} $\text{Nd}_2\text{Fe}_{14}\text{B/C}$ load density, C_d is larger and R_{ct} is lower for the magnetic electrode than the nonmagnetic electrode, and reaches the same result at 1.20 mg cm^{-2} $\text{Nd}_2\text{Fe}_{14}\text{B/C}$ load density. The magnetic electrode with 0.80 mg cm^{-2} $\text{Nd}_2\text{Fe}_{14}\text{B/C}$ load density has a larger C_d and lower R_{ct} than the magnetic electrode with 1.20 mg cm^{-2} load density. The change in C_d and R_{ct} indicates the variations of the related electrode reactions in the magnetic field. The electrode process that was susceptible to the magnetic field includes the electron, ions, and the paramagnetic oxygen transfer [18–20]. Under the steady state, the oxygen transfer speed is determined by the R_{ct} , the magnetic electrode has a smaller R_{ct} , indicating that the magnetic $\text{Nd}_2\text{Fe}_{14}\text{B/C}$ promotes the oxygen transfer process and the ORR speeds up [21].

$$C_d = \Delta j_1 / (2\nu) \quad (4)$$

$$R_{ct} = \Delta E / \Delta j_2 \quad (5)$$

where C_d is the electric double-layer capacitance; R_{ct} is the charge-transfer resistance; Δj_1 is the current change at the reversing potential; Δj_2 is the linear current change; ν is the potential scan rate, 100 V s^{-1} ; and ΔE is the potential change.

Table 1 shows that the magnetic electrode had higher C_d and lower R_{ct} than the nonmagnetic electrode. The C_d value involved the directional arrangement of hydrogen ions and electrons at the electric double layer. First, for the magnetic electrochemical systems, the magnetic dipole moment of hydrogen ions tended to align along the direction of the magnetic field lines, and the hydrogen ion convection was enhanced under the Lorentz force. Consequently, the directed hydrogen ion concentration was increased at the electrode interface [22,23]. Second, the dielectric constant of the electrolyte was enhanced at the electric double layers because the microscopic structure of the water molecules changed under the magnetic field [24]. These factors caused C_d to increase after the magnetization of magnetic particles. Under magnetic attractions, the oxygen concentration increased at the electrode interface. Therefore, the ORR rate accelerated, which caused R_{ct} to decrease as magnetic particles were magnetized.

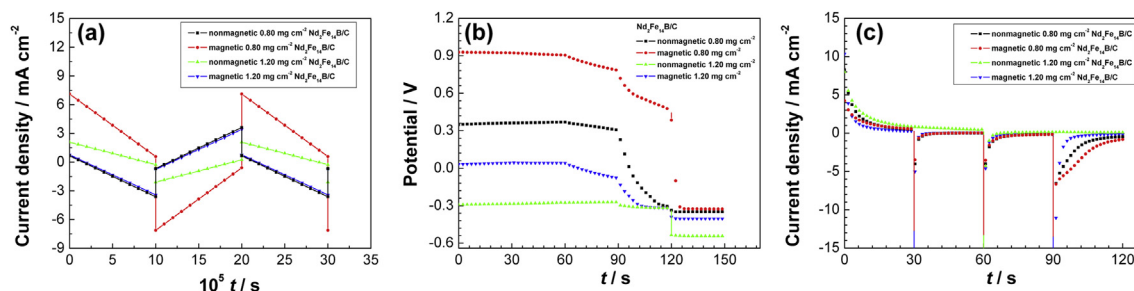


Fig. 10. Small triangular waveform linear scan (a), multi-current steps (b), and multi-potential steps (c) of the nonmagnetic and magnetic electrodes at different $\text{Nd}_2\text{Fe}_{14}\text{B/C}$ load densities. (a) Scan range, $0.80 \text{ V} - 0.79 \text{ V}$; scan rate 100 V s^{-1} . (b) Successive step, $0.01, 0.1, 1, 10, \text{ and } 100 \text{ mA}$; each step is 30 s . (c) Successive step $1.0, 0.8, 0.6, 0.4 \text{ V}$; each step is 30 s .

Table 1

Electric double-layer capacitance and charge-transfer resistance of the nonmagnetic and magnetic electrode at different Nd₂Fe₁₄B/C load densities.

	0.80 mg·cm ⁻² Nd ₂ Fe ₁₄ B/C		1.20 mg·cm ⁻² Nd ₂ Fe ₁₄ B/C	
	<i>C_d</i> /μF cm ⁻²	<i>R_{ct}</i> /Ω cm ²	<i>C_d</i> /μF cm ⁻²	<i>R_{ct}</i> /Ω cm ²
Nonmagnetic electrode	14.73	2.33	9.13	4.28
Magnetic electrode	38.48	1.53	13.25	2.40

Fig. 10(b) shows the multi-current step curve, where the polarization increased and the potential gradually decreased when the polarization current increased from −0.01 mA to −100 mA. In the same step current, the polarization of the magnetic electrode is less than that of the nonmagnetic electrode; thus, the magnetic electrode has higher potential. According to the equivalent circuit of Fig. 11, the relationship among the different electrode parameters in the non-steady state is given by Eqs. (6)–(9). In Table 1, the *C_d* of the magnetic electrode increased by 23.75 μF cm⁻² than that of the nonmagnetic electrode at 0.80 mg cm⁻² Nd₂Fe₁₄B/C load density. With the same step current and step time the magnetic electrode has a larger *C_d* according to Eq. (7), hence its interface overpotential (*η_{interface}*) is smaller. Meanwhile, the ohmic resistance overpotential (*η_R*) is a fixed value in the same three-electrode electrochemical system using Eq. (8); thus, the total overpotential (*η*) is smaller for the magnetic electrode than the nonmagnetic electrode. In Fig. 9, the magnetic electrode has higher relative equilibrium potential than the nonmagnetic electrode using Eq. (9); thus, the polarization potential is higher for the magnetic electrode. The results further show that the magnetic field generated from the Nd₂Fe₁₄B/C magnetic powder reduces the oxygen reduction overpotential (*η*), and correspondingly increases the ORR potential in the same polarization current.

$$t = 0, \eta_R = -iR_u \quad (6)$$

$$t = t1, \int i_c dt = C_d \eta_{interface} \quad (7)$$

$$\eta = \eta_R + \eta_{interface} \quad (8)$$

$$E = E_{equilibrium} + \eta \quad (\eta < 0) \quad (9)$$

Fig. 10(c) shows the multi-potential step curve at different Nd₂Fe₁₄B/C load densities, and the potential step ranges from 1.0 V to 0.40 V. The oxygen reduction current appears at *E* ≤ 0.80 V. The polarization current for the magnetic electrode is higher than the nonmagnetic electrode at Nd₂Fe₁₄B/C load density of 0.80 and 1.20 mg cm⁻². The current sudden drop at the step moment is caused by the current following properties toward the solution

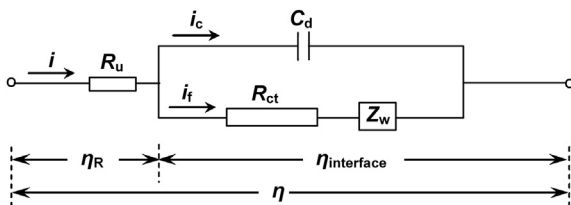


Fig. 11. Electrode equivalent circuit with the concentration polarization. Where *i*, *i_c*, and *i_t* is the polarization current, electric double-layer charging current, and ORR current, respectively; *C_d*, is the electric double-layer capacitance; *R_{ct}*, is the charge-transfer resistance; *R_u*, is the ohmic resistance; *Z_w*, is the diffusion impedance; *η_R*, is the ohmic overpotential; *η_{interface}*, is the interface overpotential; and *η*, is the total overpotential.

resistance (*R_u*), as shown in Eq. (10). For a certain potential step in the same three-electrode electrochemical system, the total overpotential (*η*) is constant. As shown in Table 1, the *C_d* at a same Nd₂Fe₁₄B/C load density is larger for the magnetic electrode than the nonmagnetic electrode. With a same polarization time, for the magnetic electrode, according to Eq. (7), the interface overpotential (*η_{interface}*) is smaller, and the total overpotential (*η*) is constant in the same electrochemical system. Therefore, using Eq. (8), the ohmic resistance overpotential (*η_R*) is larger for the magnetic electrode. According to Eq. (11), the magnetic electrode in the same step potential has larger polarization current than the nonmagnetic electrode.

$$t = 0, i = \eta/R_u \quad (10)$$

$$t = t1, i = \eta_R/R_u \quad (11)$$

3.6. Rotating disk electrode experiment

Fig. 12 shows the polarization curves of the magnetic and nonmagnetic electrode at 0.80 mg cm⁻² Nd₂Fe₁₄B/C load density. As shown in this figure, the ORR current at 1.0 V–0.98 V is irrelevant to the rotation speed, and the electrode reaction is controlled by the charge-transfer process. When the reduction potential is lower than 0.98 V, the diffusion current increases with the increase in rotation speed, and the electrode reaction is controlled by the diffusion process. According to Eqs. (12) and (13), as the rotation speed increases in the same electrochemical reaction system, the diffusion layer thickness decreases. The oxygen transfer gradient increases; thus, the oxygen diffusion current becomes larger with the increase in rotation speed [25,26].

$$\delta = 1.61D_0^{1/3} \nu^{1/6} \omega^{-1/2} \quad (12)$$

$$i = B(C_O^* - C_O^S) \omega^{1/2} \quad (13)$$

$$1/i = 1/i^e + (1/BC_O^*) \omega^{-1/2} \quad (14)$$

$$B = 0.62nFAD_0^{2/3} \nu^{-1/6} \quad (15)$$

where *δ* is the diffusion layer thickness; *D₀* is the oxygen diffusion coefficient; *ν* is the electrolyte viscosity; *ω* is the rotation speed; *i* is the polarization current; *C_O^{*}* is the oxygen concentration in the bulk solution; *C_O^S* is the oxygen concentration at the working electrode interface; *B* is a constant; and *i^e* is the ORR current without concentration polarization.

Based on the linear sweep voltammetry curves in Fig. 12, according to Eq. (14), the Koutecký–Levich curves is obtained under the magnetic and nonmagnetic conditions, as shown in Fig. 13. Using Eq. (16), the relative oxygen diffusion coefficient (*D_O*) and the average slope (*k_i*) of the Koutecký–Levich curves at Nd₂Fe₁₄B/C load density of 0.80 mg cm⁻² are calculated and listed in Table 2. The oxygen diffusion coefficient of the magnetic electrode increased by 23.5% than the nonmagnetic electrode at 0.80 mg cm⁻² Nd₂Fe₁₄B/C load density, as shown in Table 2.

$$D_{OA}/D_{OB} = (k_B/k_A)^{3/2} \quad (16)$$

where *k_i* is the slope of the Koutecký–Levich curve.

In Fig. 13, the intercept of the Koutecký–Levich curves is the ORR current (*i^e*) without concentration polarization. The Tafel curves are obtained using Eq. (17), as shown in Fig. 14. The relationship between the Tafel slope (*k_i*) and the oxygen transfer coefficient (*α_i*) are

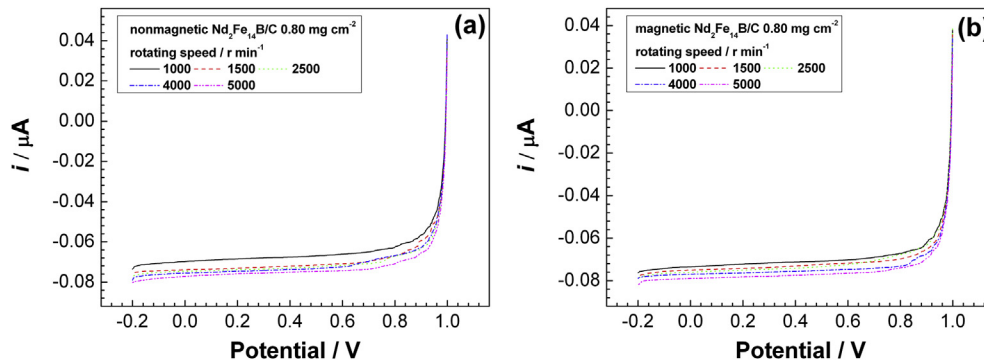


Fig. 12. Linear scan voltammograms with rotating disk electrode under nonmagnetic and magnetic conditions. (a) Nonmagnetic electrode; (b) magnetic electrode. Scan rate, 5 mV s^{-1} ; electrolyte, $0.5 \text{ M H}_2\text{SO}_4$ with air saturation.

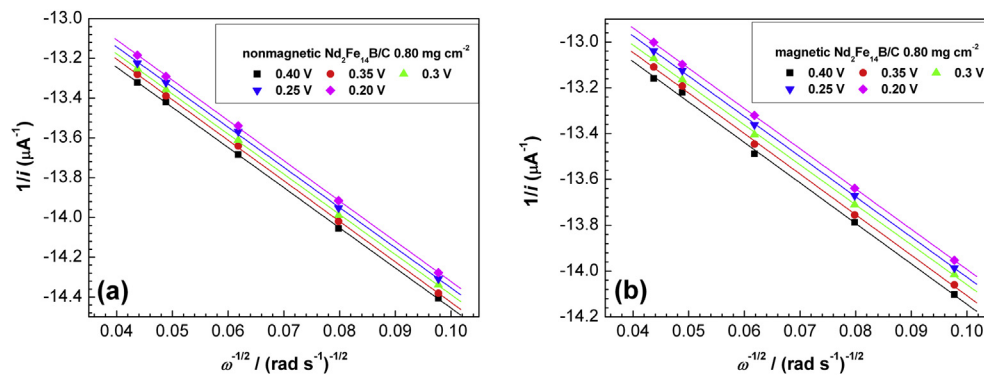


Fig. 13. Koutecký–Levich curves with rotating disk electrode under nonmagnetic and magnetic conditions. (a) Nonmagnetic electrode; (b) magnetic electrode. Scan rate, 5 mV s^{-1} ; electrolyte, $0.5 \text{ M H}_2\text{SO}_4$ with air saturation.

given in Eq. (18). The relative values of the oxygen transfer coefficient (α_i) are listed in Table 3, according to Eq. (18). At 0.80 mg cm^{-2} $\text{Nd}_2\text{Fe}_{14}\text{B/C}$ load density, the oxygen transfer coefficient (α_i) of the magnetic electrode increased by 5.9% than that of the nonmagnetic electrode, as shown in Table 3.

$$\lg i^e = -(\alpha n F / RT)E + (\alpha n F / RT)E^\theta + \lg i^\theta \quad (17)$$

$$\alpha_A / \alpha_B = k_A / k_B \quad (18)$$

where i^e is the ORR current without concentration polarization; α_i is the oxygen transfer coefficient; E is the electrode potential; E^θ is the standard electrode potential; i^θ is the exchange current density; and k_i is the slope of the Tafel curve.

The results show that the magnetic field generated from the magnetic powder promotes the oxygen transfer speed through the magnetic force toward the paramagnetic oxygen molecules. Therefore, the oxygen diffusion coefficient (D_0) is larger for the magnetic electrode. Meanwhile, the micromagnetic force increases the kinetic energy of the oxygen molecules, improving the numbers of active oxygen molecules, thereby increasing the transfer coefficient for the magnetic electrode. Dong-hyo Kim reported that the

magnetic field accelerates the oxygen molecules diffused to the electrode interface, and improves the reaction rate of the dissolved oxygen [27]. I Costa also reported that the Nd–Fe–B magnet corrosion rate is correlated with the dissolved oxygen transfer speed variations at the solution/magnet interface in the magnetic field [28].

3.7. $\text{Nd}_2\text{Fe}_{14}\text{B/C}$ magnetic powder application in PEMFC

Fig. 15(a) and (b) shows the polarization and power density curves of the magnetic and nonmagnetic PEMFC with $\text{Nd}_2\text{Fe}_{14}\text{B/C}$ in the cathode. At $\text{Nd}_2\text{Fe}_{14}\text{B/C}$ load density 0.40 and 0.80 mg cm^{-2} in

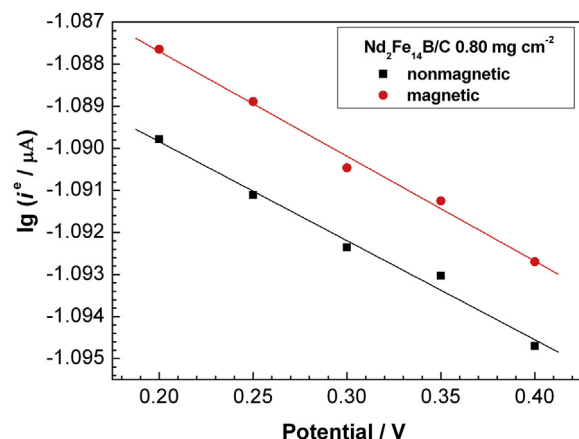


Fig. 14. Tafel curves under nonmagnetic and magnetic conditions. Scan rate, 10 mV s^{-1} ; electrolyte, $0.5 \text{ M H}_2\text{SO}_4$ with air saturation.

Table 2
Oxygen diffusion coefficient of the nonmagnetic and magnetic electrodes.

	0.80 mg cm^{-2} $\text{Nd}_2\text{Fe}_{14}\text{B/C}$	
	Nonmagnetic	Magnetic
Koutecký–Levich slope, k_i	−20.24	−17.58
Diffusion coefficient, D_0	1.000	1.235
Increase in diffusion coefficient, %	—	23.5

Table 3

Oxygen transfer coefficient of the nonmagnetic and magnetic electrodes.

	0.80 mg·cm ⁻² Nd ₂ Fe ₁₄ B/C	
	Nonmagnetic	Magnetic
Tafel slope, k_i	-0.02354	-0.02492
Transfer coefficient, α_i	1.000	1.059
Increase in transfer coefficient, %	—	5.9

the cathode, the discharge performance of the magnetic PEMFC is better than that of the nonmagnetic PEMFC. At Nd₂Fe₁₄B/C load density of 0.40 mg cm⁻² in the PEMFC cathode, the discharge current of the magnetic PEMFC was 710.67 mA cm⁻² at 0.20 V discharge voltage, which increased by 39.87% more than the nonmagnetic PEMFC (Table 4). Okada et al. reported that the discharge current of the magnetic PEMFC is 600 mA cm⁻² at 0.20 V discharge voltage after NdFeB/polyamide is loaded in PEMFC cathode. The large size of the Nd–Fe–B/polyimide particles and its insulation property constrain the magnetic PEMFC discharge performance [10]. The results showed that the discharge performance of the PEMFC can be significantly improved after Nd₂Fe₁₄B/C magnetic powder is loaded and magnetized in the PEMFC cathode. In the preparation of magnetic PEMFC, the experimental results are expected to be further improved through electrode structure optimization.

Fig. 16 shows the PEMFC open circuit voltage (OCV) curves. Here, the OCV is 0.936 V for the PEMFC without Nd₂Fe₁₄B/C in the cathode, and the magnetic PEMFC OCVs are 0.953 and 0.942 V at Nd₂Fe₁₄B/C load densities of 0.40 and 0.80 mg cm⁻², respectively. Comparison of the OCVs obtained at different Nd₂Fe₁₄B/C load densities in the PEMFC cathode showed the following pattern: OCV at 0.40 mg cm⁻² > OCV at 0.80 mg cm⁻² > OCV without Nd₂Fe₁₄B/C. The OCV of the magnetic PEMFC with 0.40 mg cm⁻² Nd₂Fe₁₄B/C increased by 11 mV compared with that of the magnetic PEMFC with 0.80 mg cm⁻² Nd₂Fe₁₄B/C and by 17 mV compared with that of the PEMFC cathode without Nd₂Fe₁₄B/C. At the same Nd₂Fe₁₄B/C load density, the magnetic PEMFC OCV was higher by 1 mV compared with the OCV of the nonmagnetic PEMFC. These results show that Nd₂Fe₁₄B/C magnetic powders can increase cathode conductivity and accelerate oxygen mass transfer, thereby improving the PEMFC discharge performance. At high load densities of the magnetic powder, reductions in the number of active Pt/C catalyst sites and decreases in the oxygen transfer efficiency in the micromagnetic field occur; thus, the PEMFC discharge performance deteriorates.

Table 4Comparison of the polarization current between the nonmagnetic and the magnetic PEMFC with different Nd₂Fe₁₄B/C load densities at the discharge voltage of 0.20 V.

	0.40 mg cm ⁻² Nd ₂ Fe ₁₄ B/C		0.80 mg cm ⁻² Nd ₂ Fe ₁₄ B/C		Without Nd ₂ Fe ₁₄ B/C
	Nonmagnetic	Magnetic	Nonmagnetic	Magnetic	
Discharge current, mA cm ⁻²	508.08	710.67	311.01	454.67	205.36
Increase in discharge current, %	—	39.874	—	46.191	—

Fig. 17 shows variations in the PEMFC response voltage with the pulse current. The pulse current amplitude differs according to the PEMFC discharge performance. As shown in Fig. 17(a) and (b), at a Nd₂Fe₁₄B/C load density of 0.40 mg cm⁻², the pulse current amplitude as well as the response voltage of the magnetic PEMFC are higher than those of the nonmagnetic PEMFC. The magnetic PEMFC discharge voltage is 0.313 V at 26 s duration and 720 mA cm⁻² pulse current. Similarly, in Fig. 17(c) and (d), the discharge performance of the magnetic PEMFC is higher than that of the nonmagnetic PEMFC. Fig. 17(d) shows the PEMFC response voltage obtained without Nd₂Fe₁₄B/C in the cathode. Compared with the magnetic and nonmagnetic PEMFCs, the response voltage dropped quickly with increasing pulse current in the absence of Nd₂Fe₁₄B/C. The discharge voltage was 0.162 V at 26 s duration and 140 mA cm⁻² pulse current. The experimental results further show that the presence of a certain amount of Nd₂Fe₁₄B/C magnetic powders of the cathode can significantly improve the PEMFC discharge performance.

In contrast of the magnetic PEMFC discharge performance at different Nd₂Fe₁₄B/C load densities, the discharge performance at 0.40 mg cm⁻² load density is better than at 0.80 mg cm⁻² load density, which may be attributed to several reasons. First, the carbon particles in the magnetic materials enhance the cathode conductivity at the lower load density, thereby, reducing the cathode ohmic polarization. Second, more paramagnetic oxygen molecules move to the Pt/C catalyst surface under the magnetic attractions; thus, the discharge performance is enhanced. When the magnetic powder load density is higher, on the one hand, the oxygen transfer channel blockage becomes severe because the Nd₂Fe₁₄B/C particle coverage on Pt/C catalytic site reduces the Pt/C active catalytic area. On the other hand, at the higher Nd₂Fe₁₄B/C load density, the

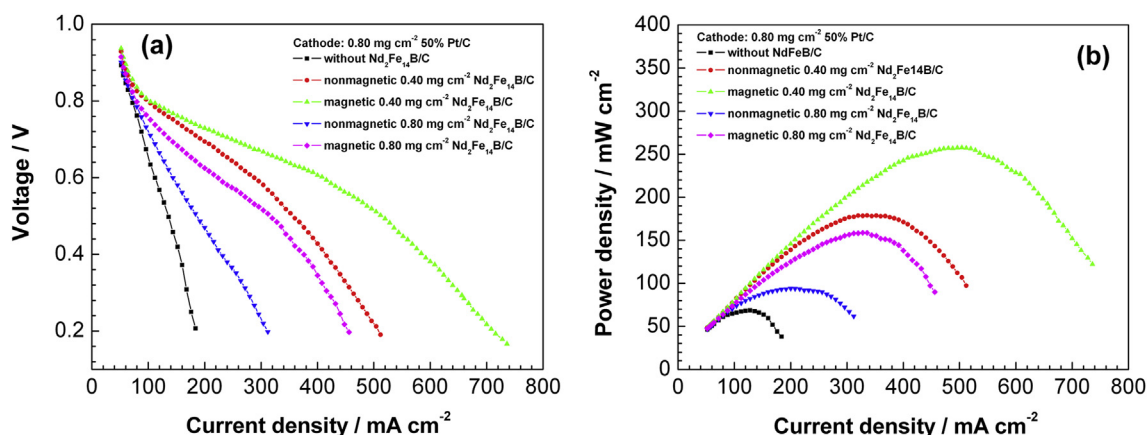


Fig. 15. Polarization (a) and power density (b) curves of the nonmagnetic and magnetic PEMFC at different Nd₂Fe₁₄B/C load densities in the cathode. Cell temperature, 70 °C; humidifier temperature, 70 °C; hydrogen and air entrance pressure, 0.11 MPa.

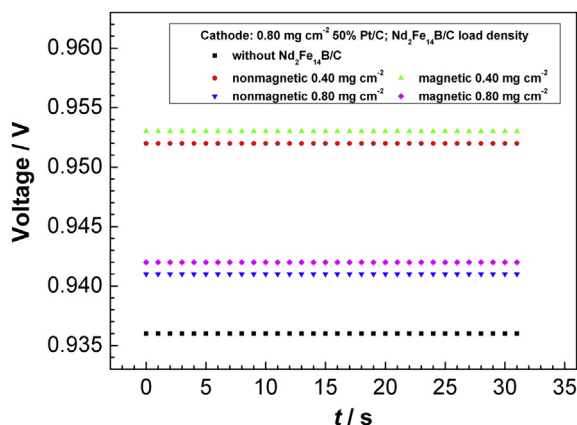


Fig. 16. Open circuit voltage curves obtained from PEMFC cathodes with different $\text{Nd}_2\text{Fe}_{14}\text{B}/\text{C}$ load densities under magnetic and nonmagnetic conditions. Cell temperature, 70 °C; humidifier temperature, 70 °C; hydrogen and air entrance pressure, 0.11 MPa.

magnetic interactions among different magnetic particles reduce the orderly magnetic field of the single magnetic particles, which weaken the oxygen transfer efficiency in the magnetic field, thereby decreasing the magnetic PEMFC discharge performance.

4. Conclusions

The $\text{Nd}_2\text{Fe}_{14}\text{B}/\text{C}$ magnetic material plays a positive role in the ORR process. Compared with the nonmagnetic electrode, the micro-magnetic field of the magnetic electrode increases the C_d and decreases the R_{ct} in the ORR process. The magnetic electrode polarization decreases and the oxygen reduction potential increases in the same polarization current.

The oxygen diffusion coefficient and transfer coefficient both increased for the magnetic electrode. The oxygen transfer speed improves in the micro-magnetic field generated from the magnetic powders. The magnetic force improves the kinetic energy of the oxygen molecules. Therefore, the ORR rate was higher in the magnetic electrode than the nonmagnetic electrode.

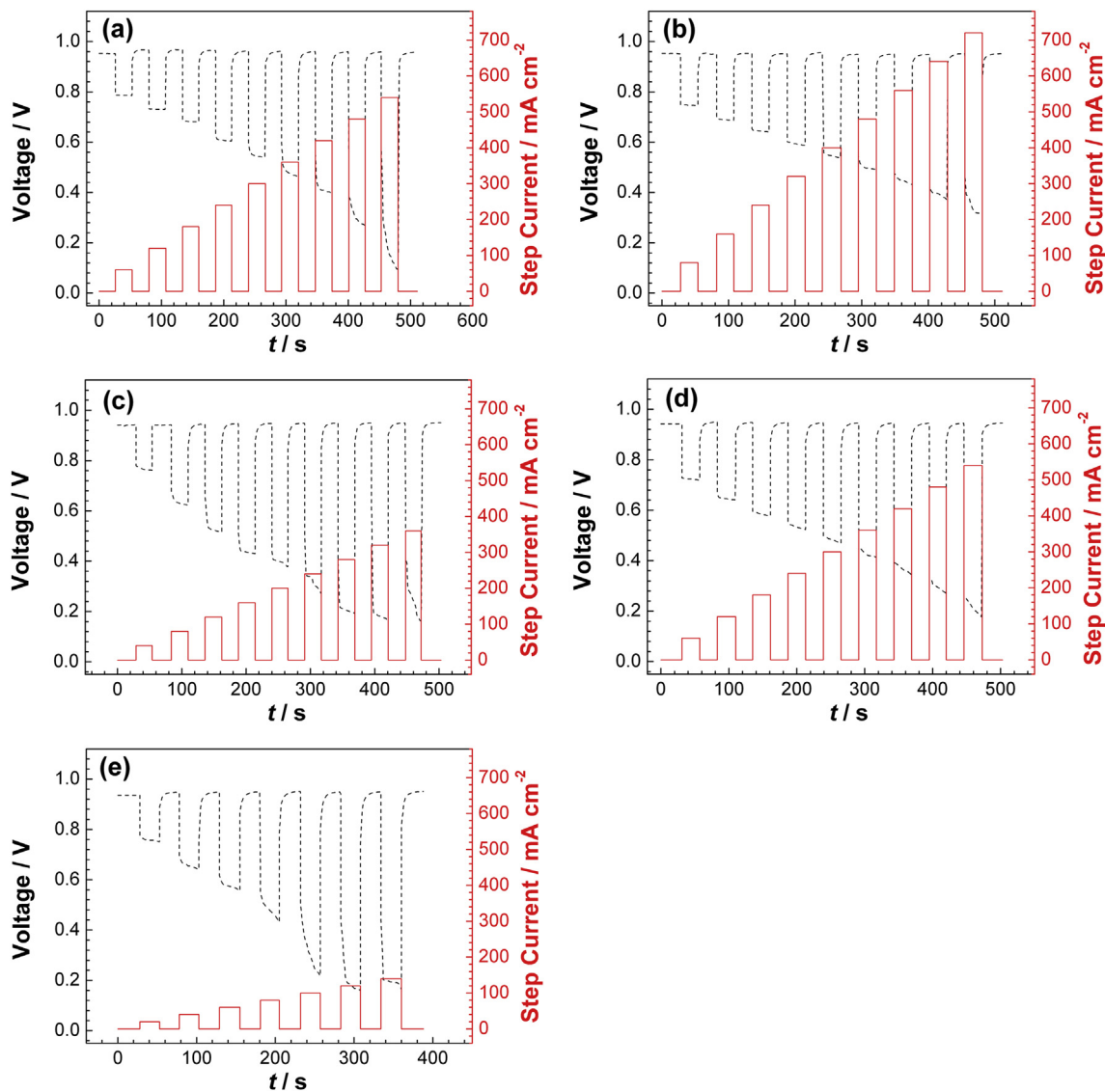


Fig. 17. Response voltage curves and pulse currents obtained from PEMFC cathodes with different $\text{Nd}_2\text{Fe}_{14}\text{B}/\text{C}$ load densities under magnetic and nonmagnetic conditions. (a) Nonmagnetic PEMFC with 0.40 mg cm^{-2} $\text{Nd}_2\text{Fe}_{14}\text{B}/\text{C}$ in the cathode; (b) magnetic PEMFC with 0.40 mg cm^{-2} $\text{Nd}_2\text{Fe}_{14}\text{B}/\text{C}$ in the cathode; (c) nonmagnetic PEMFC with 0.80 mg cm^{-2} $\text{Nd}_2\text{Fe}_{14}\text{B}/\text{C}$ in the cathode; (d) magnetic PEMFC with 0.80 mg cm^{-2} $\text{Nd}_2\text{Fe}_{14}\text{B}/\text{C}$ in the cathode; (e) no $\text{Nd}_2\text{Fe}_{14}\text{B}/\text{C}$ in the PEMFC cathode. Cell temperature, 70 °C; humidifier temperature, 70 °C; hydrogen and air entrance pressure, 0.11 MPa.

Given that the $\text{Nd}_2\text{Fe}_{14}\text{B}/\text{C}$ load density is lower in PEMFC cathode, the carbon particles in $\text{Nd}_2\text{Fe}_{14}\text{B}/\text{C}$ magnetic powder enhance the cathode conductivity and decrease the cathode ohmic polarization. Meanwhile, the micro-magnetic field generated from the magnetic powder promotes the oxygen transfer process; thus, the discharge performance of the magnetic PEMFC is better than the nonmagnetic electrode.

When the magnetic powder load density is higher in the PEMFC cathode, the oxygen transfer channel blockage becomes the dominated factors. In addition, the ordered magnetic field of the single particle is impaired by the magnetic force interactions among different magnetic particles. Therefore, the PEMFC discharge performance decreases because of the deteriorated oxygen transfer efficiency in the higher $\text{Nd}_2\text{Fe}_{14}\text{B}/\text{C}$ load density.

Acknowledgments

This research was funded by the National Basic Research Program of China (No. 2012CB215500, Program 973) and the National Natural Science Foundation of China (No. 21176035).

References

- [1] Y. Nagahara, S. Sugawara, K. Shinohara, *J. Power Sources* 182 (2008) 422–428.
- [2] J. Cai, L. Wang, P. Wu, *Phys. Lett. A* 362 (2007) 105–108.
- [3] A. Rybak, Z.J. Grzywna, W. Kaszuwara, *J. Membr. Sci.* 336 (2009) 79–85.
- [4] L.B. Wang, N.I. Wakayama, T. Okada, *Chem. Eng. Sci.* 60 (2005) 4453–4467.
- [5] J.M. Hu, X.L. Liu, J.Q. Zhang, C.N. Cao, *Prog. Org. Coat.* 55 (2006) 388–392.
- [6] L.Z. Song, Z.Y. Yang, *J. Iron Steel Res. Int.* 16 (2009) 89–94.
- [7] W.T. He, L.Q. Zhu, H.N. Chen, H.Y. Nan, W.P. Li, H.C. Liu, Y. Wang, *Appl. Surf. Sci.* 279 (2013) 416–423.
- [8] X.G. Liu, S.W. Or, S.L. Ho, D.Y. Geng, Z.G. Xie, H. Wang, Z.D. Zhang, *J. Alloys Compd.* 509 (2011) 2929–2932.
- [9] G. Bai, R.W. Gao, Y. Sun, G.B. Han, B. Wang, *J. Magn. Magn. Mater.* 308 (2007) 20–23.
- [10] T. Okada, N.I. Wakayama, L.B. Wang, H. Shingu, J. Okano, T. Ozawa, *Electrochim. Acta* 48 (2003) 531–539.
- [11] B. Merzougui, A. Hachimi, A. Akinpelu, S. Bukola, M.H. Shao, *Electrochim. Acta* 107 (2013) 126–132.
- [12] R. Othman, A.L. Dicks, Z.H. Zhu, *Int. J. Hydrogen Energy* 37 (2012) 357–372.
- [13] B. Wang, *J. Power Sources* 152 (2005) 1–15.
- [14] J.C. Shi, H.F. Xu, L. Lu, X. Sun, *Electrochim. Acta* 90 (2013) 44–52.
- [15] Z.P. Lu, W. Yang, *Corros. Sci.* 50 (2008) 510–522.
- [16] T.N. Tuan, Y. Yi, J.K. Lee, J. Lee, *Catal. Today* 216 (2013) 240–245.
- [17] H. Sakurai, H. Yasui, K. Kunitomi, M. Kamatari, N. Kaneko, A. Nakayama, *Pathophysiology* 7 (2000) 93–99.
- [18] K.T. Chang, C.I. Weng, *Comput. Mater. Sci.* 43 (2008) 1048–1055.
- [19] I. Bica, *J. Ind. Eng. Chem.* 15 (2009) 605–609.
- [20] S. Aoyagi, A. Yano, Y. Yanagida, E. Tanihira, A. Tagawa, M. Iimoto, *Chem. Phys.* 331 (2006) 137–141.
- [21] J.H. Zeng, S.J. Liao, J.Y. Lee, Z.X. Liang, *Int. J. Hydrogen Energy* 35 (2010) 942–948.
- [22] N. Khare, P. Singh, J.K. Vassiliou, *J. Power Sources* 218 (2012) 462–473.
- [23] J.A. Koza, M. Uhlemann, A. Gebert, L. Schultz, *J. Electroanal. Chem.* 617 (2008) 194–202.
- [24] X.F. Pang, B. Deng, *Phys. B (Amsterdam Neth.)* 403 (2008) 3571–3577.
- [25] A.J. Martín, A.M. Chaparro, M.A. Folgado, J. Rubio, L. Daza, *Electrochim. Acta* 54 (2009) 2209–2217.
- [26] D.J. Yang, B. Li, H. Zhang, J.X. Ma, *Int. J. Hydrogen Energy* 37 (2012) 2447–2454.
- [27] D.H. Kim, J.W. Kim, W.Y. Choi, *J. Hazard. Mater.* 192 (2011) 928–931.
- [28] I. Costa, M.C.L. Oliveira, H.G. de Melo, R.N. Faria, *J. Magn. Magn. Mater.* 278 (2004) 348–358.